ARTICLES
https://doi.org/10.1038/s41563-019-0320-9
nature materials

Ultrahigh conductivity in Weyl semimetal NbAs nanobelts

Cheng Zhang[1,2,14], Zhuoliang Ni[1,2,14], Jinglei Zhang[3,14], Xiang Yuan[1,2,14], Yanwen Liu[1,2], Yichao Zou[4], Zhiming Liao[4], Yongping Du[5], Awadhesh Narayan[6], Hongming Zhang[1,2], Tiancheng Gu[1,2], Xuesong Zhu[1,2], Li Pi[3], Stefano Sanvito[7], Xiaodong Han[8], Jin Zou[4,9], Yi Shi[2,10], Xiangang Wan[2,11], Sergey Y. Savrasov[12] and Faxian Xiu[1,2,13]*

In two-dimensional (2D) systems, high mobility is typically achieved in low-carrier-density semiconductors and semimetals. Here, we discover that the nanobelts of Weyl semimetal NbAs maintain a high mobility even in the presence of a high sheet carrier density. We develop a growth scheme to synthesize single crystalline NbAs nanobelts with tunable Fermi levels. Owing to a large surface-to-bulk ratio, we argue that a 2D surface state gives rise to the high sheet carrier density, even though the bulk Fermi level is located near the Weyl nodes. A surface sheet conductance up to 5–100 S per □ is realized, exceeding that of conventional 2D electron gases, quasi-2D metal films, and topological insulator surface states. Corroborated by theory, we attribute the origin of the ultrahigh conductance to the disorder-tolerant Fermi arcs. The evidenced low-dissipation property of Fermi arcs has implications for both fundamental study and potential electronic applications.

Electric transport properties of low-dimensional systems have been one of the central topics of condensed matter physics in the last two decades[1–3]. Such intense interests are driven by both fundamental study and functional nanoscale device research. Significant advances have been made in low-carrier-density systems such as carbon-based low-dimensional structures[2] and quantum wells[1], in which high sample quality and tunability of electronic properties can be easily accessed. In contrast, much less progress has been made in the study of high-carrier-density systems, owing to the lack of good low-dimensional metals. Conventional bulk metals suffer from surface roughness and defects when made into the nanoscale, while most layered metallic materials are found to be unstable. Doping/gating low-carrier-density systems into high-carrier-density metals[1,2,4] is gradually being adopted as a common approach but additional scattering may be induced and degrade the mobility value, hindering the study of intrinsic properties in low-dimensional metals.

Recently, Weyl semimetals have been discovered as a new group of topological materials[5–10]. In Weyl semimetals, conduction and valence bands touch at discrete points in the Brillouin zone, forming quasiparticles that can be described by the Weyl equation[5,6]. The band touching points, or Weyl nodes, can be regarded as monopoles for Berry curvature. By breaking either time-reversal symmetry[5] or inversion symmetry[6], Weyl nodes with opposite chirality can be separated in momentum space. Gapless boundary states then emerge on the surface of Weyl semimetals, manifesting themselves as arc-like states connecting the surface projection of Weyl node pairs[5]. Many exotic phenomena have been observed in Weyl semimetals, such as chiral anomaly[11–14], Weyl orbits[15,16] and anomalous Hall effect[17]. Apart from these physical properties, the intriguing properties of Weyl fermions have also stimulated extensive studies towards the realization of functionalities such as magnetization switching[18] and valley polarization[19]. Apart from the bulk state, the surface Fermi arc is also predicted to host low-dissipation transport[20,21] with exotic helical spin texture[6], which may be a good candidate for a clean 2D metal.

Despite the rapid progress in investigating the physical properties of bulk Weyl semimetals, the research of surface-state transport and related device physics has been limited by the lack of an ideal material system with clean band structure and easy integration into nanoscale devices. One important reason is that most Weyl semimetals discovered so far involve heavy transition metals[9], which typically show low vapour pressure and are therefore difficult to grow through conventional thin film synthesis techniques, such as molecular beam epitaxy and pulsed laser deposition. In particular, the widely studied transition metal pnictide TaAs family (TaAs, NbAs, TaP and NbP) suffers from the high evaporation temperature of Ta/Nb and the complicated phase diagram of Ta–As compounds. Top-down methods such as focused ion beam etching result in Ta/Nb residues, owing to the significant difference of the surface binding energy[22]. In contrast, layered materials such as $WTe_2/MoTe_2$[23] are dominated by trivial carriers rather than Weyl fermions in transport, although they can be exfoliated into micro size. Hence, unlike the Dirac semimetals Cd_3As_2

[1]State Key Laboratory of Surface Physics and Department of Physics, Fudan University, Shanghai, China. [2]Collaborative Innovation Center of Advanced Microstructures, Nanjing, China. [3]Anhui Province Key Laboratory of Condensed Matter Physics at Extreme Conditions, High Magnetic Field Laboratory of the Chinese Academy of Sciences, Hefei, China. [4]Materials Engineering, The University of Queensland, Brisbane, Queensland, Australia. [5]Department of Applied Physics and Institution of Energy and Microstructure, Nanjing University of Science and Technology, Nanjing, China. [6]Materials Theory, ETH Zurich, Zurich, Switzerland. [7]School of Physics and CRANN Institute, Trinity College, Dublin, Ireland. [8]Beijing Key Laboratory and Institute of Microstructure and Property of Advanced Materials, Beijing University of Technology, Beijing, China. [9]Centre for Microscopy and Microanalysis, The University of Queensland, Brisbane, Queensland, Australia. [10]School of Electronic Science and Engineering, Nanjing University, Nanjing, China. [11]National Laboratory of Solid State Microstructures, School of Physics, Nanjing University, Nanjing, China. [12]Department of Physics, University of California, Davis, Davis, CA, USA. [13]Institute for Nanoelectronic Devices and Quantum Computing, Fudan University, Shanghai, China. [14]These authors contributed equally: Cheng Zhang, Zhuoliang Ni, Jinglei Zhang, Xiang Yuan. *e-mail: Faxian@fudan.edu.cn

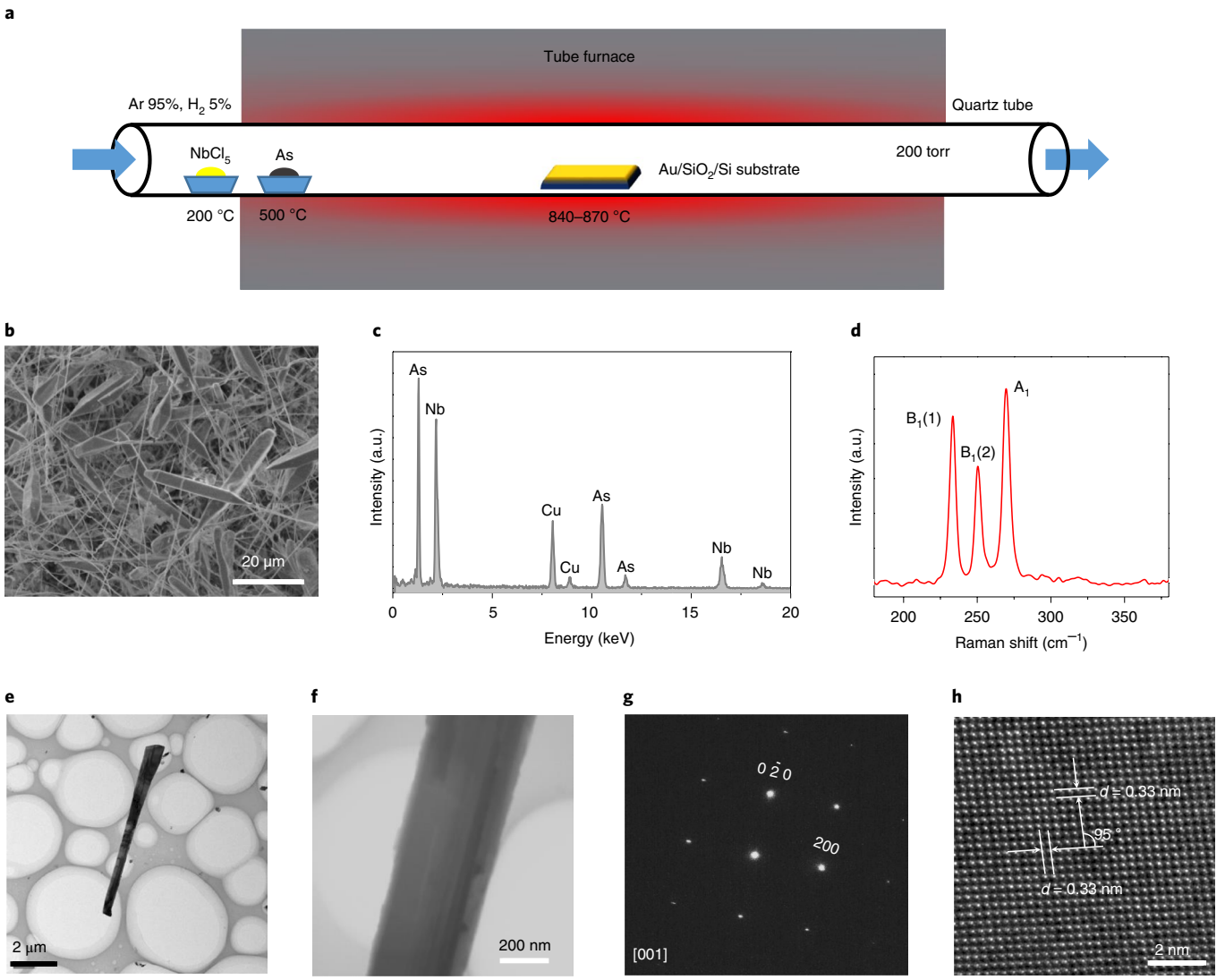

Fig. 1 | Growth and characterization of NbAs nanobelts. a, Illustration of the CVD growth process of NbAs nanobelts using a horizontal tube furnace. **b**, A SEM image of the as-grown NbAs nanobelts and nanowires on SiO_2/Si substrate. **c**, The corresponding EDS spectrum acquired during the TEM measurements. The Cu peaks come from the copper grid. **d**, The Raman spectrum of the NbAs nanobelts, in which three phonon modes can be identified. **e**,**f**, TEM images showing a typical nanobelt on a copper grid (**e**) and its enlarged section (**f**). **g**, The corresponding SAED pattern of **f**. **h**, [1$\bar{1}$1] zone-axis high-resolution TEM image of a NbAs nanobelt showing high crystalline quality.

and $ZrTe_5$, the mesoscopic transport of Weyl semimetals remains largely unresolved.

Here, we report the synthesis of NbAs nanobelts by chemical vapour deposition (CVD) technique and investigate the transport properties of the as-grown nanobelts. To overcome the high evaporation temperature problem mentioned above, we use the metal chlorides ($NbCl_5$) to react with hydrogen as the Nb source. As illustrated in Fig. 1a, NbAs is formed by heating $NbCl_5$ and As vapours to 840–870 °C along with H_2 gas as the reducing agent in a low-pressure CVD system (see Methods for details). A thin gold layer (~15 nm) is pre-coated on the substrate, acting as the catalyst. Figure 1b is a scanning electron microscopy (SEM) image taken from the obtained NbAs nanobelts and nanowires. We also performed energy dispersive spectroscopy (EDS) analysis to determine the chemical composition of the NbAs nanobelts (note that the Cu peak is due to the Cu grid which supports the nanobelts during transmission electron microscopy (TEM) experiments). The corresponding EDS spectrum indicates that the atomic ratio between Nb and As is close to 1:1 (Fig. 1c). Also, the EDS mapping shows a uniform distribution of Nb/As elements (Supplementary Fig. 1). Figure 1d shows the Raman spectrum taken from the NbAs nanobelts. As for NbAs bulk crystals, three peaks are resolved, corresponding to the $B_1(1)$, $B_1(2)$ and A_1 modes, respectively. Figure 1e displays the TEM image of a NbAs nanobelt on the copper grid. Figure 1f is an enlarged section of the nanobelt and Fig. 1g is the corresponding selective area electron diffraction (SAED) pattern, consistent with the body-centred tetragonal structure of NbAs. Since the SAED pattern was taken on a nanobelt without any tilting and it is the [001] zone-axis, the pattern indicates that the belt has a large fraction of (001) surfaces. Figure 1h is a high-resolution TEM image viewed along the [1$\bar{1}$1] zone-axis, revealing the perfect crystal structure of the as-grown NbAs nanobelt with a lattice constant of 0.33 nm. The thickness of the nanobelts and the diameter of the nanowires are usually around several tens to a few hundred nanometres. In this study, we focus on the transport properties of NbAs nanobelts with a well-defined (001) belt surface. Samples with a thickness in the range of 100–300 nm (Supplementary Table 1) are specifically chosen to enhance the surface-state transport

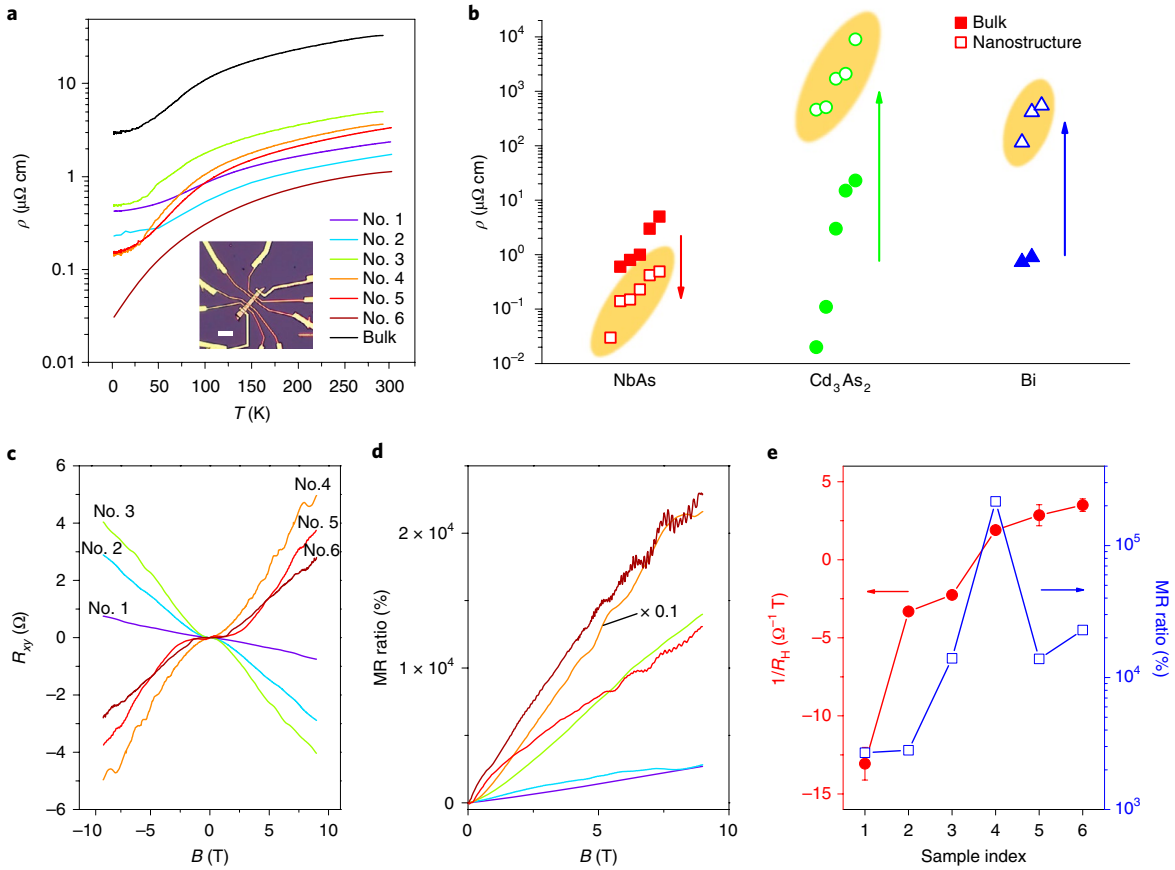

Fig. 2 | Transport data for a series of NbAs nanobelts. a, The temperature (T) dependence of the overall resistivity in NbAs nanobelts (samples 1–6). In comparison, the resistivity of bulk NbAs (the black curve) is also displayed, which is over one order of magnitude larger. The inset is an optical image of a typical NbAs nanobelt device used to study the transport properties. Scale bar, 20 μm. **b**, A comparison of bulk and nanostructure resistivity (ρ) in three representative semimetals, NbAs, Cd_3As_2 and Bi. Part of the data (including NbAs bulk, Cd_3As_2/Bi bulk and nanostructures) is taken from the literature[16,27,29,35–38]. The data points for each material are separated along the x axis only for clarity. **c**,**d**, The Hall resistance R_{xy} (**c**) and relative magnetoresistance (MR) ratio (**d**) of a series of NbAs nanobelts as a function of magnetic field, B. The samples are indexed in the order of n-type to p-type transition. **e**, The inverse of the extracted Hall coefficient R_H and the MR ratio at 9 T. The MR ratio is found to achieve the maximum value near the n-to-p transition. R_H is estimated using a linear fit to the R_{xy}–B curve to describe the overall trend, with the error bars from the standard error of the linear fit.

while preventing the bulk band structure from the quantum confinement effect.

Transport experiments were carried out in a series of NbAs nanobelts (thickness shown in Supplementary Table 1). Figure 2a summarizes the temperature dependence of the resistivity in these nanobelts, along with another set of data from bulk NbAs for comparison. The inset of Fig. 2a shows a typical device fabricated using an as-grown nanobelt. All of them show a metallic behaviour with a very small residue resistivity in the range of 0.03–2 μΩ cm at low temperatures. Interestingly, the overall resistivity value is more than one order of magnitude smaller than that of the bulk counterpart. This is anomalous because the carriers experience more boundary scatterings in nanoscale samples. Normally this will result in a substantial increase in resistivity owing to the decrease in mobility[3]. Such behaviour is particularly true when it comes to high mobility semimetal systems, such as Weyl semimetals, where the original mean free path of carriers is very long (up to micrometre range), exceeding the confined geometry. Figure 2b presents a direct comparison of the resistivity in bulk crystals and nanostructures of three representative systems, namely NbAs, Cd_3As_2 and Bi. All three materials have a semimetallic band structure with a similar carrier density of ~10^{18} cm^{-3} and a high mobility over 10,000 $cm^2V^{-1}s^{-1}$. In contrast to NbAs, the resistivity in Cd_3As_2 nanoplates and Bi thin films is nearly two orders of magnitude larger than that of their bulk crystals, as one would normally expect. As a simple comparison, with a similar thickness of around 100 nm, the sheet resistance of NbAs and Cd_3As_2 is of the order of ~0.01 Ω and ~50 Ω, respectively. It is also worthwhile mentioning that the room-temperature conductivity of NbAs nanobelts is even comparable to that of conventional bulk metals such as copper, gold and silver[24].

To determine the origin of the anomalous decrease of resistivity in NbAs nanobelts, we measured the Hall effect and magnetoresistance as shown in Fig. 2c–e. The change of Hall coefficient from negative to positive value suggests a crossover of the dominant carriers from n- to p-type. Here, the Hall coefficient, as summarized in Fig. 2e, is estimated by performing a linear fit over the entire magnetic field (B) range. These samples are obtained from slightly different growth conditions with the deposition temperature varying between 840 °C and 870 °C. Higher deposition temperature tends to yield p-type carriers. In fact, the change of carrier type originates from the semimetallic band structure. In previous photoemission experiments[25], the Fermi level of NbAs was found to be close to the Weyl nodes. Different growth conditions may shift the Fermi level, resulting in the change of the carrier type, as has been observed in TaAs bulk crystals[26]. A similar transport behaviour, as shown in Fig. 2c, suggests that the Fermi level in our NbAs nanobelts is also near the Weyl nodes, which enables easy switching between the conduction and valence bands. Similar to bulk NbAs[27], the magnetoresistance

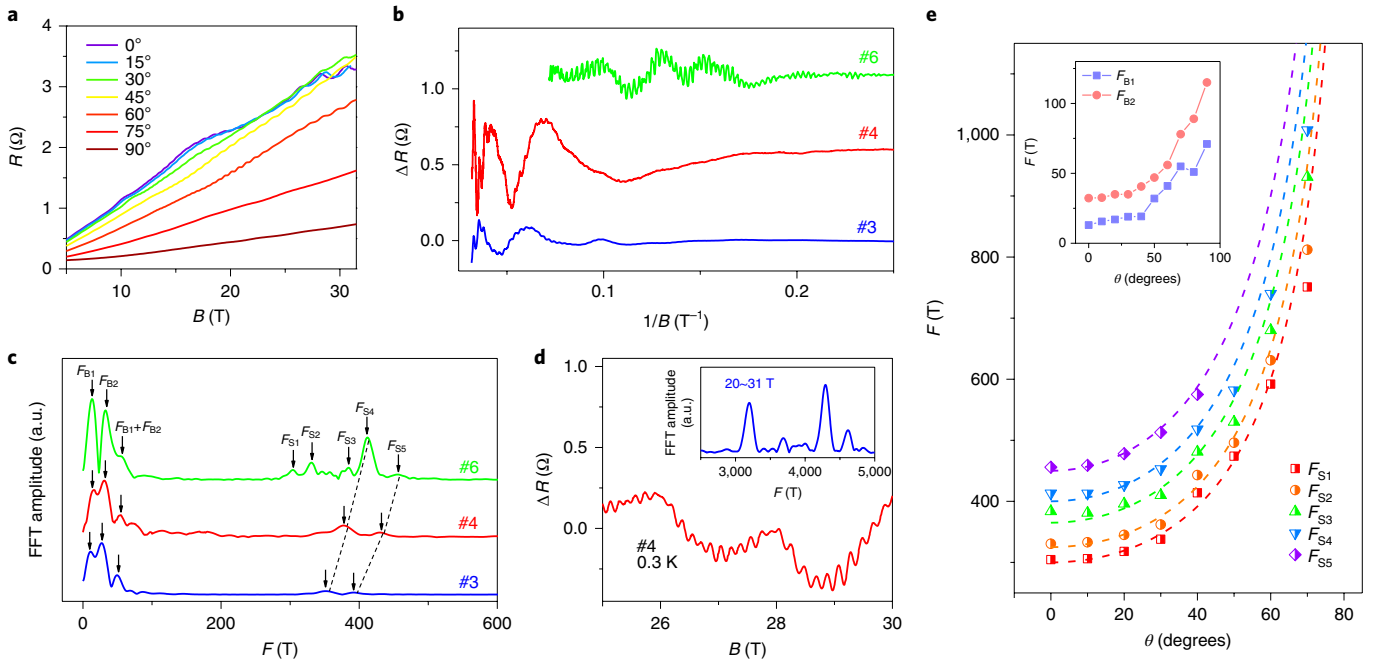

Fig. 3 | Quantum oscillation analysis and the Fermi surface in NbAs nanobelts. a, Angle dependence of magnetoresistance (MR) in sample 3 in high magnetic fields up to 31.5 T. **b**, Quantum oscillations extracted from MR in samples 3 and 6. Fast surface quantum oscillations are found to be superimposed on the slow bulk quantum oscillations. **c**, The FFT spectra of the quantum oscillations with corresponding frequencies *F* marked. $F_{B1}+F_{B2}$ corresponds to the harmonic frequency of two bulk oscillations F_{B1} and F_{B2}. **d**, The high-frequency oscillations of sample no. 4. The inset is the FFT result of the corresponding oscillations within the range of 20–31 T. **e**, The angle dependence of oscillation frequencies. The inset shows two low frequencies corresponding to anisotropic 3D Fermi surfaces, while all the higher frequencies follow the expectations of 2D behaviour up to a field angle θ of ~45°, although F_{s1}–F_{s4} slightly deviate from the 2D expectation at larger θ.

ratio in nanobelts, defined as $R(B)/R(0)-1$, is also very large, of the order of 10^3–10^5 (Fig. 2d). Figure 2e plots the inverse of Hall coefficient $1/R_H$ and magnetoresistance ratio of different samples. The magnetoresistance ratio is found to reach a maximum value around the n-to-p transition. At the same time, quantum oscillations can be observed in both magnetoresistance and Hall resistivity, with the amplitude becoming stronger in p-type samples. Here, the Hall coefficient reveals a much higher carrier concentration in nanobelts than in bulk crystals of the TaAs family[26,28], for example, 8.1×10^{15} cm^{-2} for sample no. 1 and ~10^{13} cm^{-2} for bulk carriers with a thickness of 100 nm. According to previous transport experiments[29,30], the Fermi surface of NbAs bulk crystals with (001) surface only shows two sets of oscillations with close frequency around 20 T from the two kinds of Weyl nodes. In contrast, here in samples 5 and 6, in addition to the low-frequency components, a series of high-frequency oscillations are observed (Fig. 2d). They correspond to the emergence of very large Fermi surfaces other than those originating from the Weyl cones. Furthermore, the beating pattern of the high-frequency oscillations indicates the coexistence of multiple orbits. Note that such fast oscillations have never been detected in bulk NbAs[30]. It is well known that in nanostructures the surface-state component will be enhanced due to the large surface-to-bulk ratio. Thin films and nanobelts have been widely used in the study of the surface states in topological insulators[31] and most recently in Dirac semimetals[16]. Therefore, the observed high-frequency oscillations and low resistivity could come from the surface states, which were overwhelmed and thus undetected in previous transport experiments based on bulk crystals.

To track the dimensionality of the additional large Fermi surface, we further carried out a magnetotransport experiment in high magnetic fields for three representative samples, no. 3 (n-type), no. 4 and no. 6 (p-type). Figure 3a shows the magnetoresistance of sample no. 3 with magnetic field tilting from 0° (out-of-plane) to 90° (in-plane). High-frequency oscillations are observed above 10 T and disappear as the field is tilted towards the in-plane direction. The oscillations extracted from the magnetoresistance R_{xx} (0°) are shown in Fig. 3b. The fast oscillations are superimposed onto the slow ones. Figure 3c–e presents the corresponding fast Fourier transform (FFT) spectra of the oscillation patterns and the angle dependence of the oscillation frequencies, respectively. In both samples, two low-frequency components, marked as F_{B1} and F_{B2}, are observed. Their values and anisotropic properties (inset of Fig. 3e and Supplementary Fig. 4) are consistent with previously reported bulk Fermi surfaces of NbAs crystals[29,30]. The frequency of F_{B1} and F_{B2} become smaller in samples 3 and 4, suggesting that the Fermi energy is lower. Five additional frequencies (F_{S1}–F_{S5}) are resolved in the FFT analysis of sample no. 6 while only two exist in samples 3 and 4 in the range of 200–600 T. By tracking the angle dependence (Fig. 3e), we find that they have the angular dependence expected of a 2D state for field angle θ less than 45°. Although deviations from perfect 2D behaviour are seen for larger values of θ (refer to Section IV of Supplementary Information for more discussion), the oscillations disappear when θ approaches 90°, consistent with the property of the surface state. Under the perpendicular magnetic field, the size of cyclotron orbits (F_{S1}–F_{S5}) is in the range of 0.029–0.044 Å^{-2} (300–460 T). Compared with previous Fermi surfaces determined from photoemission experiments[25], such orbits may correspond to the Fermi arcs of Weyl nodes W2 close to the Brillouin zone centre in terms of the enclosed area. However, these orbits form only a small part of the entire Fermi-arc contour. In addition to F_{S1}–F_{S5}, we find that another four sets of fast oscillations with even higher frequencies (3,000–5,000 T; Fig. 3d) above 20 T in sample 4 by measuring it at lower temperatures down to 0.3 K. The total area from the six surface cyclotron orbits in sample 4 is 1.44 Å^{-2}. Considering a degeneracy of 2 from

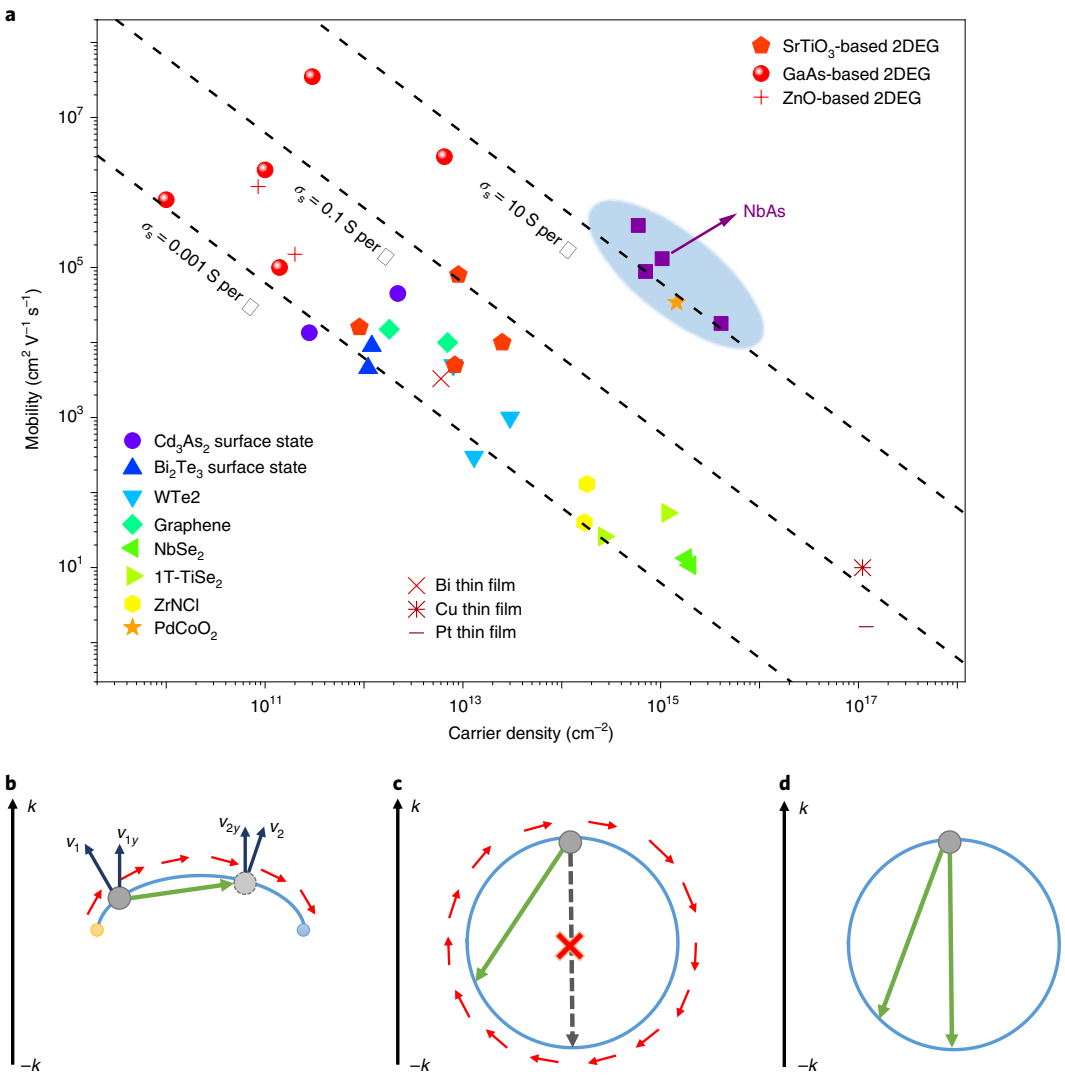

Fig. 4 | A comparison of sheet conductance among various 2D systems and the illustration of scattering mechanisms. a, Comparison of the carrier density–mobility scaling among various 2D systems. The surface state of NbAs nanobelts is found to host the largest sheet conductivity. The three dashed lines correspond to three sheet conductance values. Data of other materials are taken from the literature with a typical thickness below 20 nm and measured below 10 K[4,16,31–33,35,39–50]. **b**–**d**, The scattering processes in the momentum (k) space for the Fermi arc (**b**), topological insulator surface state (**c**) and conventional Fermi pocket without spin texture (**d**), respectively. The red, blue and green arrows indicate the spin texture, the velocities and the possible scattering vectors, respectively. The initial and final states of intra-arc scattering give similar momentum directions. The spin-independent backscattering is strictly forbidden in the topological insulator surface state due to the helical spin texture.

the in-plane mirror symmetry, this corresponds to a sheet carrier density of $7.3\times10^{14}\,cm^{-2}$, quite close to the measured Hall carrier density of sample 4 ($5.9\times10^{14}\,cm^{-2}$). The four orbits in the range of 3,000–5,000 T (Fig. 3d) provide the majority of the surface carriers. In Section V of Supplementary Information, we rule out the possibility of anisotropic bulk Fermi surfaces as the origin of these high-frequency quantum oscillations. Owing to the high carrier density from the surface state, we anticipate that even in NbAs samples with a thickness of tens of micrometres, the surface transport will still have a detectable impact on the Hall signal. As presented in Section VI of Supplementary Information, the Hall resistivity indeed shows a systematic trend with the thickness in polished NbAs microflakes. The thickness dependence of the Hall coefficient also allows us to estimate a surface carrier density of $3.2\times10^{15}\,cm^{-2}$, within the range of the carrier density of NbAs nanobelts (Fig. 4a).

Having established the surface state as the origin of high conductance in NbAs nanobelts, we now go back to re-evaluate the transport properties within the framework of 2D systems. By comparing with bulk, we know that the sheet carrier density, as well as the high conductivity in NbAs nanobelts, is mainly contributed by the surface state. The corresponding sheet conductance (per surface) and carrier mobility at 2 K are in the range of 5–100 S per □ and $1.5-35\times10^4\,cm^2V^{-1}s^{-1}$, respectively. Note that here we do not include the data of samples 5 and 6 since the one-carrier approximation may yield large errors in determining the carrier density in these two samples. In Sections II and III of Supplementary Information, we show other ways to calculate the mobility and the transport results of NbAs nanowires to further verify the high mobility in NbAs nanobelts. To get a better idea of these values, we compare them with other common 2D/quasi-2D conductors in a carrier density–mobility scaling plot, as shown in Fig. 4a. Here, we include conventional three-dimensional (3D) metals grown as ultrathin films or nanostructure forms, intrinsic layered materials in the 2D limit and quantum well systems. To the best of our knowledge, the NbAs surface state provides one of the highest sheet conductance values among all these 2D

systems, over two orders of magnitude larger than typical 2D metals and previously studied topological surface states (generally below 0.1 S per □). In comparison to 3D bulk materials, 2D systems tend to show lower mobility owing to various extrinsic and intrinsic effects, such as surface roughness, boundary scattering and enhanced localization[1]. High-quality quantum well systems can overcome these mobility limits by confining carriers within two large potential barriers. However, the generated carrier density, typically around $10^{12}\,cm^{-2}$, is usually low compared with metals, thus limiting the conductance. Although high-carrier-density 2D electron gases have been made using d-electron systems such as $SrTiO_3$ (10^{13}–$10^{15}\,cm^{-2}$)[32,33], the mobility is in turn significantly degraded owing to the large charged impurity scattering. Here, the Weyl semimetal surface states can overcome such a trade-off. Physically, we expect that the Fermi-arc surface state is capable of supporting strong surface currents because the corresponding wave functions extend well into the bulk near the Weyl points, making them robust against disorder. Their scattering cross-sections on impurities or phonons are generally similar to the case of 3D topological insulators, whose surface states consist of massless 2D Dirac fermions with the helical orientation of spins at a circular Fermi surface. This spin–momentum locking in 3D topological insulators results in the suppression of 180 degrees backscattering from non-magnetic impurities, since states with opposite spin and momentum remain orthogonal. While there is no general spin–momentum locking mechanism for the Fermi-arc states of Weyl semimetals, backscattering of electrons from the arc associated with the top surface to the arc associated with the bottom surface is also forbidden due to zero spatial overlap between the corresponding electronic states.

There is, however, another important difference between a circular Fermi surface of a 3D topological insulator and a disconnected Fermi arc of a Weyl semimetal that originates in phase space availability for the transitions between scattered electrons in transport calculations[21]. Under applied external field in a certain direction α, the matrix element for the electron at state k to scatter to the state k' at the Fermi surface is weighted by the electron velocities pre-factor $(v_{k\alpha} - v_{k'\alpha})^2$ appearing as a generalization of a famous $(1-\cos\theta_{k-k'})$ for free electrons[34]. For the disconnected arcs, the velocities of the electrons projected onto the direction of the current remain similar before and after scattering, which makes the surface resistivity tremendously reduced for the curved arc in general, and vanishingly small in the limit of a straight arc geometry. This conclusion is virtually independent of the particular form of the scattering cross-sections, but results from the fact that, in the limit of a straight arc, scattering only occurs between states with the same velocity along the direction of the current. Figure 4b–d summarizes the scattering processes in a Fermi arc, a topological insulator surface state and a conventional Fermi pocket, respectively. The intra-arc scattering only slightly tilts the direction without strongly affecting the transport lifetime in a Fermi arc, as shown in Fig. 4b. Meanwhile, it results in a small value of $(v_{1y} - v_{2y})^2$ between the initial and final states. In a toplogical insulator surface state, although the momentum-reversal-type backscattering is strictly prohibited during the spin-independent scattering process[10], the oblique backward scattering (indicated by the green arrow in Fig. 4c) is still possible. Finally, in a conventional Fermi pocket, scattering along all directions is allowed (Fig. 4d). Therefore, we can expect a long transport lifetime from Fermi arcs even in the presence of strong electron–electron scattering. For the real material NbAs studied here, there is a multiplicity of arcs that necessarily leads to the inter-arc scattering of the electrons. However, this should not strongly affect the broadening of the Fermi arcs and their transport, since the arcs are rather compact in k-space, and such scattering events are rare due to a requirement of a finite momentum transfer corresponding to wave vectors that separate the arcs.

Our recent theoretical work simulating the effect of surface vacancies on the Fermi arcs in an almost identical system, TaAs[21], revealed that the arc states acquire very little broadening up to very high values of surface disorders. This is primarily attributed to a very small strength in hybridization of the surface states with the remaining electrons. This hybridization strength is at the heart of the impurity problem that appears when evaluating the disorder-induced self-energies using a Coherent Potential Approximation, a self-consistent theory that we used to investigate the effect of quenched surface vacancies on the Fermi arcs electronic spectral functions. The resulting calculations of surface conductivity using Kubo–Greenwood formalism showed a great insensitivity to disorder, which is interpreted as driven primarily by the disorder-tolerant Fermi-arc electrons. Thus, we can expect a high carrier mobility from these Fermi arcs since they have a small effective mass and a low scattering rate. Indeed, the estimated carrier mobility (Fig. 4a and Supplementary Fig. 2d) is comparable to that of the bulk Weyl fermions in the TaAs family[28,29]. In contrast, the large curvature of Fermi arcs[7,8,25] gives rise to the exceptional large density of states as detected here, even when the Fermi level is close to the Weyl nodes. The 24 Weyl nodes in this material result in multiple sets of Fermi arcs widely distributed over the whole Brillouin zone. This unique feature actually helps to minimize the scattering between Fermi arcs and bulk electrons, since the projection of bulk Fermi surface on the surface state is small. The coexistence of high carrier density and high mobility in the NbAs surface state results in a large sheet conductance, as observed in the experiments. In contrast, Cd_3As_2 nanostructures show much smaller sheet conductance of $0.5–10\times10^{-2}$ S per □ owing to the low carrier density ($10^{12}\,cm^{-2}$) from the short Fermi arcs[16,35].

In conclusion, we successfully synthesized high-quality NbAs nanobelts using CVD and discovered ultrahigh conductivity from the surface state. This growth method can be easily extended to other transition metal pnictides and enables further studies towards the exotic transport properties of Fermi arcs. The high conductance of NbAs surface states may also facilitate Weyl semimetal-based electronic applications such as thermoelectric conversion and supercapacitors.

Online content

Any methods, additional references, Nature Research reporting summaries, source data, statements of data availability and associated accession codes are available at https://doi.org/10.1038/s41563-019-0320-9.

Received: 14 June 2018; Accepted: 11 February 2019;
Published online: 18 March 2019

References

1. Ando, T., Fowler, A. B. & Stern, F. Electronic properties of two-dimensional systems. *Rev. Mod. Phys.* **54**, 437–672 (1982).
2. Das Sarma, S., Adam, S., Hwang, E. H. & Rossi, E. Electronic transport in two-dimensional graphene. *Rev. Mod. Phys.* **83**, 407–470 (2011).
3. Beenakker, C. & van Houten, H. Quantum transport in semiconductor nanostructures. *Solid State Phys.* **44**, 1–228 (1991).
4. Ye, J. T. et al. Liquid-gated interface superconductivity on an atomically flat film. *Nat. Mater.* **9**, 125–128 (2009).
5. Wan, X., Turner, A. M., Vishwanath, A. & Savrasov, S. Y. Topological semimetal and Fermi-arc surface states in the electronic structure of pyrochlore iridates. *Phys. Rev. B* **83**, 205101 (2011).
6. Weng, H., Fang, C., Fang, Z., Bernevig, B. A. & Dai, X. Weyl semimetal phase in noncentrosymmetric transition-metal monophosphides. *Phys. Rev. X* **5**, 011029 (2015).
7. Lv, B. Q. et al. Experimental discovery of Weyl semimetal TaAs. *Phys. Rev. X* **5**, 031013 (2015).
8. Xu, S.-Y. et al. Discovery of a Weyl fermion semimetal and topological Fermi arcs. *Science* **349**, 613–617 (2015).
9. Armitage, N. P., Mele, E. J. & Vishwanath, A. Weyl and Dirac semimetals in three-dimensional solids. *Rev. Mod. Phys.* **90**, 015001 (2018).

10. Zhang, C., Lu, H.-Z., Shen, S.-Q., Chen, Y. P. & Xiu, F. Towards the manipulation of topological states of matter: a perspective from electron transport. *Sci. Bull.* **63**, 580–594 (2018).
11. Xiong, J. et al. Evidence for the chiral anomaly in the Dirac semimetal Na_3Bi. *Science* **350**, 413–416 (2015).
12. Li, Q. et al. Chiral magnetic effect in $ZrTe_5$. *Nat. Phys.* **12**, 550–554 (2016).
13. Zhang, C. et al. Room-temperature chiral charge pumping in Dirac semimetals. *Nat. Commun.* **8**, 13741 (2017).
14. Zhang, C. L. et al. Signatures of the Adler-Bell-Jackiw chiral anomaly in a Weyl fermion semimetal. *Nat. Commun.* **7**, 10735 (2016).
15. Moll, P. J. W. et al. Transport evidence for Fermi-arc-mediated chirality transfer in the Dirac semimetal Cd_3As_2. *Nature* **535**, 266–270 (2016).
16. Zhang, C. et al. Evolution of Weyl orbit and quantum Hall effect in Dirac semimetal Cd_3As_2. *Nat. Commun.* **8**, 1272 (2017).
17. Liang, T. et al. Anomalous Hall effect in $ZrTe_5$. *Nat. Phys.* **14**, 451–455 (2018).
18. Kurebayashi, D. & Nomura, K. Voltage-driven magnetization switching and spin pumping in Weyl semimetals. *Phys. Rev. Appl.* **6**, 044013 (2016).
19. Jiang, Q.-D., Jiang, H., Liu, H., Sun, Q.-F. & Xie, X. C. Topological Imbert-Fedorov shift in Weyl semimetals. *Phys. Rev. Lett.* **115**, 156602 (2015).
20. Gorbar, E. V., Miransky, V. A., Shovkovy, I. A. & Sukhachov, P. O. Origin of dissipative Fermi arc transport in Weyl semimetals. *Phys. Rev. B* **93**, 235127 (2016).
21. Resta, G., Pi, S.-T., Wan, X. & Savrasov, S. Y. High surface conductivity of Fermi-arc electrons in Weyl semimetals. *Phys. Rev. B* **97**, 085142 (2018).
22. Bachmann, M. D. et al. Inducing superconductivity in Weyl semimetal microstructures by selective ion sputtering. *Sci. Adv.* **3**, e1602983 (2017).
23. Ali, M. N. et al. Large, non-saturating magnetoresistance in WTe_2. *Nature* **514**, 205–208 (2014).
24. Matula, R. A. Electrical resistivity of copper, gold, palladium, and silver. *J. Phys. Chem. Ref. Data* **8**, 1147–1298 (1979).
25. Xu, S.-Y. et al. Discovery of a Weyl fermion state with Fermi arcs in niobium arsenide. *Nat. Phys.* **11**, 748–754 (2015).
26. Zhang, C.-L. et al. Electron scattering in tantalum monoarsenide. *Phys. Rev. B* **95**, 085202 (2017).
27. Ghimire, N. J. et al. Magnetotransport of single crystalline NbAs. *J. Phys. Condens. Matter* **27**, 152201 (2015).
28. Shekhar, C. et al. Extremely large magnetoresistance and ultrahigh mobility in the topological Weyl semimetal candidate NbP. *Nat. Phys.* **11**, 645–649 (2015).
29. Luo, Y. et al. Electron-hole compensation effect between topologically trivial electrons and nontrivial holes in NbAs. *Phys. Rev. B* **92**, 205134 (2015).
30. Moll, P. J. W. et al. Magnetic torque anomaly in the quantum limit of Weyl semimetals. *Nat. Commun.* **7**, 12492 (2016).
31. Xiu, F. et al. Manipulating surface states in topological insulator nanoribbons. *Nat. Nanotechnol.* **6**, 216–221 (2011).
32. Caviglia, A. D. et al. Two-dimensional quantum oscillations of the conductance at $LaAlO_3/SrTiO_3$ interfaces. *Phys. Rev. Lett.* **105**, 236802 (2010).
33. Matsubara, Y. et al. Observation of the quantum Hall effect in δ-doped $SrTiO_3$. *Nat. Commun.* **7**, 11631 (2016).
34. Ziman, J. M. *Electrons and Phonons: The Theory of Transport Phenomena in Solids* (Oxford Univ. Press, 1960).
35. Schumann, T. et al. Observation of the quantum Hall effect in confined films of the three-dimensional Dirac semimetal Cd_3As_2. *Phys. Rev. Lett.* **120**, 016801 (2018).
36. Liang, T. et al. Ultrahigh mobility and giant magnetoresistance in the Dirac semimetal Cd_3As_2. *Nat. Mater.* **14**, 280–284 (2015).
37. Du, X., Tsai, S.-W., Maslov, D. L. & Hebard, A. F. Metal-insulator-like behavior in semimetallic bismuth and graphite. *Phys. Rev. Lett.* **94**, 166601 (2005).
38. Yang, F. Y. et al. Large magnetoresistance of electrodeposited single-crystal bismuth thin films. *Science* **284**, 1335–1337 (1999).
39. Fatemi, V. et al. Magnetoresistance and quantum oscillations of an electrostatically tuned semimetal-to-metal transition in ultrathin WTe_2. *Phys. Rev. B* **95**, 041410 (2017).
40. Zhang, Y., Tan, Y. W., Stormer, H. L. & Kim, P. Experimental observation of the quantum Hall effect and Berry's phase in graphene. *Nature* **438**, 201–204 (2005).
41. Xi, X., Berger, H., Forró, L., Shan, J. & Mak, K. F. Gate tuning of electronic phase transitions in two-dimensional $NbSe_2$. *Phys. Rev. Lett.* **117**, 106801 (2016).
42. Qu, D.-X., Hor, Y. S., Xiong, J., Cava, R. J. & Ong, N. P. Quantum oscillations and Hall anomaly of surface states in the topological insulator Bi_2Te_3. *Science* **329**, 821–824 (2010).
43. Li, L. J. et al. Controlling many-body states by the electric-field effect in a two-dimensional material. *Nature* **529**, 185–189 (2015).
44. Kane, B. E., Pfeiffer, L. N., West, K. W. & Harnett, C. K. Variable density high mobility two-dimensional electron and hole gases in a gated $GaAs/Al_xGa_{1-x}As$ heterostructure. *Appl. Phys. Lett.* **63**, 2132–2134 (1993).
45. Tsui, D. C., Stormer, H. L. & Gossard, A. C. Two-dimensional magnetotransport in the extreme quantum limit. *Phys. Rev. Lett.* **48**, 1559–1562 (1982).
46. Joseph, F. & Masashi, K. A review of the quantum Hall effects in MgZnO/ZnO heterostructures. *Rep. Prog. Phys.* **81**, 056501 (2018).
47. Lu, M. et al. Low-temperature electrical-transport properties of single-crystal bismuth films under pressure. *Phys. Rev. B* **53**, 1609–1615 (1996).
48. Van den dries, L., Van Haesendonck, C., Bruynseraede, Y. & Deutscher, G. Two-dimensional localization in thin copper films. *Phys. Rev. Lett.* **46**, 565–568 (1981).
49. Markiewicz, R. S. & Harris, L. A. Two-dimensional resistivity of ultrathin metal films. *Phys. Rev. Lett.* **46**, 1149–1153 (1981).
50. Umansky, V. et al. MBE growth of ultra-low disorder 2DEG with mobility exceeding $35{\times}10^6$ cm^2/Vs. *J. Cryst. Growth* **311**, 1658–1661 (2009).

Acknowledgements

F.X. was supported by National Natural Science Foundation of China (grant nos. 61322407, 11474058, 61674040 and 11874116), National Key Research and Development Program of China (grant nos. 2017YFA0303302 and 2018YFA0305601) and the National Young 1000 Talent Plan. Part of the sample fabrication was performed at Fudan Nano-fabrication Laboratory. Part of the transport measurements was performed at the High Magnetic Field Laboratory, CAS. A portion of this work was performed at the National High Magnetic Field Laboratory (USA), which is supported by the National Science Foundation (NSF) cooperative agreement no. DMR-1644779, no. DMR-1157490 and the State of Florida. S.Y.S. was supported by NSF DMR (grant no. 1411336). Australian Research Council and Australian Microscopy and Microanalysis Research Facility are acknowledged for supporting the nano-characterization. A.N. acknowledges support from ETH Zurich. S.S. acknowledges support from Science Foundation Ireland (14/IA/2624 and 16/US-C2C/3287). Part of the computations were carried out at the Trinity Centre for High-Performance Computing. J.Z. was supported by Youth Innovation Promotion Association CAS (grant no. 2018486), the Innovative Program of Development Foundation of Hefei Center for Physical Science and Technology (grant no. 2017FXCX001), and the Scientific Instrument Developing Project of the Chinese Academy of Sciences (grant no.YJKYYQ20180059). C.Z. and X.Y. were supported by China Scholarships Council (CSC) (grant nos. 201706100053 and 201706100054). F.X. acknowledges the tremendous help from Y. Chen for TEM characterization in Beijing University of Technology. C.Z. thanks Y. Ding for insightful discussions.

Author contributions

F.X. conceived the ideas and supervised the overall research. Z.N. synthesized NbAs nanobelts with help from C.Z., T.G., H.Z. and X.Z. C.Z. and Z.N. fabricated the devices. C.Z., X.Y. and Y.L. carried out the transport measurements assisted by J.Z. and L.P. X.Y., Y.Z., Z.L., X.H. and J.Z. performed the sample characterization. C.Z. analysed the transport data. Y.D., X.W., A.N., S.S. and S.Y.S. provided the theoretical support. C.Z., S.Y.S. and F.X. wrote the paper with help from all other co-authors.

Competing interests

The authors declare no competing interests.

Additional information

Supplementary information is available for this paper at https://doi.org/10.1038/s41563-019-0320-9.

Reprints and permissions information is available at www.nature.com/reprints.

Correspondence and requests for materials should be addressed to F.X.

Publisher's note: Springer Nature remains neutral with regard to jurisdictional claims in published maps and institutional affiliations.

Methods

Material growth and characterization. The NbAs nanobelts were grown using $NbCl_5$ powders and As chunks as the precursor in a horizontal tube furnace with a mixture of argon (95%) and hydrogen (5%) as the carrier gas (Fig. 1a). The SiO_2/Si substrates were deposited with a thin gold layer (~15 nm) to achieve the vapour–liquid–solid growth process, and they were placed in the centre of the furnace. During the growth, the temperature was first increased to 840–870 °C in 50 min, held for 15 min and then decreased to 700 °C in 30 min, before naturally cooling down to room temperature. Higher growth temperature tends to achieve p-type samples with a larger mobility. The flow rate of the carrier gas was set to 50 standard cubic centimetres per minute and the pressure was fixed at 200 Torr during the growth. After growth, the substrates appear to be silver-grey in colour by naked eye. Both nanobelts and nanowires can be found on the substrates by the optical microscope. Increasing the initial gold coating thickness to 40 nm will only result in the growth of nanowires. The morphological, structural and chemical characteristics of the as-grown NbAs nanobelts were investigated by SEM (JEOL 7800 and 7001) and TEM (FEI Titan 80–300 and Philips F20). The EDS measurement was performed in TEM. The largest surface of as-grown NbAs nanobelts was determined to be (001). The Raman spectrum was measured in a home-built Raman system with an excitation wavelength of 532.8 nm. Compared with previous work[51] on CVD growth of group Vb phosphides, the current method yields high-quality single crystals of nanostructures.

Device fabrication and transport measurements. The devices used for transport experiments were fabricated by the electron beam lithography technique and etched by standard buffered HF solution for ~5 s before depositing on electrodes. Magnetotransport with a low field regime (<9 T) was carried out in a Physical Property Measurement System (Quantum Design) with lock-in amplifiers. The high field magnetotransport was carried out in the High Magnetic Field Laboratory (CAS, China) and National High Magnetic Field Laboratory (USA).

Comparison of resistivity and the mobility–carrier density scaling. The comparison of bulk and nanostructure resistivity in three representative semimetals, NbAs, Cd_3As_2 and Bi, is presented in Fig. 2b. The thickness of nanostructures is chosen to be around or below a few hundreds of nanometres. Note that in these topological semimetals, the carrier mobility and density can be quite sensitive to the defect level, which varies with different growth conditions[26]. Therefore, the resistivity in these systems shows a wide range across several orders of magnitude. But, overall, the resistivity of NbAs shows an anomalous decrease in the nanobelt form compared with that of bulk NbAs, in contrast to Cd_3As_2 and Bi.

In high mobility topological semimetals, the current-jetting effect has been found to result in artificial changes of magnetoresistivity and Hall resistivity (for example, a 'fake' negative magnetoresistivity)[52,53]. It comes from the redistribution of current density in real space when the magnetic field is parallel with the electrical current (no Lorentz force is present). However, in the current measurement set-up, the resistivity is measured at either zero field or transverse field geometry. The longitudinal magnetoresistivity is only used for extracting the oscillation frequency for the in-plane magnetic field. Hence, the current-jetting effect should not affect the current analysis.

In Fig. 2a, we show the comparison of the carrier density–mobility scaling among various 2D systems. The surface state of NbAs nanobelts is found to host the largest sheet conductivity. The effective penetration depth of surface states is also in this range. The mobility values of Cu and Pt thin films are estimated from the thin film sheet resistance by assuming the same carrier density as their bulk. In this scaling plot, GaAs-based two-dimensional electron gas (2DEG) systems also show a high sheet conductance value close to that of NbAs surface state by modifying the growth condition to achieve an ultrahigh mobility[50]. The high mobility of 2DEG originates from the fact that the carriers are confined within a 2D plane formed by the high potential barrier in the interface of a semiconductor heterostructure. Therefore, they are less sensitive to the boundary scattering or surface defect, which is one of the important reasons for the degrading of mobility in nanostructures. However, further doping these 2DEG systems by chemical methods will induce extra scatterings from charged impurities. Hence, 2DEG systems can achieve a higher mobility than our current NbAs samples but the overall conductivity is comparably lower. We note that in recent years, the delafossite layered oxide, $PdCoO_2$, was also found to host high conductivity with suppressed scattering rate and long mean free path at low temperatures[54,55]. The extracted 2D sheet conductivity is close to the value from NbAs surface states. The quasi-2D crystal structure may play an important role in the suppression of electron scattering in $PdCoO_2$ (ref. [55]).

Data availability

The data that support the plots within this paper and other findings of this study are available from the corresponding author upon reasonable request.

References

51. Blackman, C. et al. Chemical vapour deposition of group Vb metal phosphide thin films. *J. Mater. Chem.* **13**, 1930–1935 (2003).
52. Arnold, F. et al. Negative magnetoresistance without well-defined chirality in the Weyl semimetal TaP. *Nat. Commun.* **7**, 11615 (2016).
53. Liang, S. et al. Experimental tests of the chiral anomaly magnetoresistance in the Dirac-Weyl semimetals Na_3Bi and GdPtBi. *Phys. Rev. X* **8**, 031002 (2018).
54. Moll, P. J. W., Kushwaha, P., Nandi, N., Schmidt, B. & Mackenzie, A. P. Evidence for hydrodynamic electron flow in $PdCoO_2$. *Science* **351**, 1061–1064 (2016).
55. Mackenzie, A. P. The properties of ultrapure delafossite metals. *Rep. Prog. Phys.* **80**, 032501 (2017).